Cronfa - Swansea University Open Access Repository

Self-consistent modelling of tunnelling spectroscopy on III-V semiconductors

O. Kryvchenkova,[1a] R. J. Cobley[1], K. Kalna[2]

[1]*Multidisciplinary Nanotechnology Centre, College of Engineering, Singleton Park, Swansea, SA2 8PP, United Kingdom*
[2]*Electronic Systems Design Centre, College of Engineering, Singleton Park, Swansea, SA2 8PP, United Kingdom*

A simulation methodology to model tunnelling spectroscopy measurements based on the Price-Radcliffe formalism has been developed within a finite element device simulator. The tip-sample system is modelled self-consistently including tip-induced bending and realistic tip shapes. The resulting spectra of III-V semiconductors are compared against experimental results and a model based on the Bardeen tunnelling approach with very good agreement. We have found that the image force induced barrier lowering increases the tunnelling current by three orders of magnitude when tunnelling to the sample valence band, and by six orders of magnitude when tunnelling to the sample conduction band. The work shows that other models which use a single weighting factor to account for image force in the conduction and valence band are likely to be underestimating the valence band current by three orders of magnitude.

Keywords: scanning tunnelling spectroscopy, tip induced band bending, image force

[a] Electronic mail: o.kryvchenkova.672217@swansea.ac.uk

1. Introduction

As the active regions of electronic materials and devices reduce in size to the nanoscale, the analysis tools applied to them need to be able to characterise with a spatial resolution at the same length scale. Scanning probe microscopy (SPM) is one such technique and can be used to make surface electronic, morphological, optical, chemical and magnetic measurements down to the atomic scale [1]. Unlike most electron microscopy techniques, SPM can be applied to biased devices under operation [2–5]. The main limitation of the method is that with all SPM techniques the probe can interact electrostatically and physically with the sample, changing the measured properties of the device under test [6]. Modelling the electrostatic probe interaction can be used to quantify the measurement error, to match experimental results to device properties, or potentially to remove the effects of probe interaction [7–11].

In this work, we have developed a simulation methodology to reproduce the scanning tunnelling spectroscopy (STS) and microscopy (STM) process using the simulation tool *ATLAS* by Silvaco [12]. The developed methodology allows correct modelling of the bandgap for the variety of semiconductor materials, and includes the effect of the tip induced band bending. Our method allows modelling SPM on devices, including a complete treatment of the whole device structure, with simultaneous self-consistent solutions of the device operation with the probe interaction across the whole device. The developed methodology also allows realistic tip geometries including contaminated tips, and is readily adapted to study the probe-sample interaction in all SPM techniques. It can recover STM affected data enabling to study a range of semiconductor devices including quantum well lasers [13], photovoltaic devices [14], resonant tunnelling diodes [15] and semiconductor sensors [16]. The simulation of the quantum tunnelling between the metal probe and the surface of the semiconductor is performed self-consistently, i.e., the electrostatic potential is obtained in an iterative process in which the solution of Poisson's equation follows the calculation of the tunnelling current until convergence is achieved. The methodology includes also the effect of the barrier lowering due to image force on the tunnelling of electrons and holes. In the past, approximate approaches to compensate for the image force induced barrier lowering were applied equally to the conduction and valence band [17–19]. Following work by Schenk [20], we include a complete calculation of the image force effect in our model, which will later show that equal barrier height lowering in both the conduction and valence band is not appropriate and can miscalculate the tunnelling current by orders of magnitude. Finally, this study focuses on technologically relevant III-V materials including GaAs, InP, $Al_{0.3}Ga_{0.7}As$, $In_{0.53}Ga_{0.47}As$ and GaP. Although these ideally have a flat defect free (110) surface the developed methodology also allows for the inclusion of surface states.

In general, a number of approaches and computational techniques exists to estimate quantitatively the tip induced band bending on semiconductor surfaces by solving Poisson's equation in 1D [21–24], 2D [25] and 3D [26]. First-principles calculations such as density functional theory (DFT) [27–29] are often used to calculate bandstructure of the semiconductor surface under the STS. However, the DFT can be used to model only small systems of atoms, but it is not suitable for the tasks where the whole device structure needs to be included in the calculations. In addition to the limitation to a small number of atoms, the DFT is based on a single electron approximation [30,31] and the assumption that there is a link between density and the exact ground state energy. Consequently, the calculation of excited states is cumbersome and computationally expensive when a flexible basis is needed to simultaneously describe the ground and excited states. Therefore, the DFT can model atomic scale bandstructure, but our approach, based on the multidimensional device simulator, is more computationally suitable technique for the study of the 10-100 nm systems, as typical for studying device surfaces, where atomic level perturbation becomes negligible. Instead, the behaviour of large area of the surface which is electrostatically affected has to be taken into

account. Therefore, Coulomb interactions are included within a model of the whole device structure and with the simultaneous tip-sample tunnelling [32,33]. In addition, the effect of the barrier lowering due to the image force is of the many body nature of the tip-sample system. The effect can be included in the DFT via an exchange-correlation potential [27], but only approximately at large computational costs. The computation of the tunnelling current is often based on the transfer-Hamiltonian formalism [34,35] and is used for quantitative and qualitative tunnelling current evaluation [17,36–38].

The developed simulation methodology for modelling STS in this work uses a direct quantum tunnelling model based on Price and Radcliffe's formalism [39]. A detailed explanation of the model is given in Section 2. The developed methodology which allows for any tip shape is described in Section 3. We have verified our approach by modelling the tunnelling spectroscopy process to study the bandgap for a set of III-V technologically important semiconductor bulk materials: GaAs (Section 3), InP, $Al_{0.3}Ga_{0.7}As$, $In_{0.53}Ga_{0.47}As$ and GaP (Appendix A). To estimate the validity of the results of the 2D finite element solution, we compare the computation results for p-GaAs with the experimental data and model implemented by Feenstra [17], as this model has a good agreement with experimental data and is widely accepted and used by other researchers [2,40]. The examination of a role of the image force correction can be found in Section 5 and conclusions are drawn in Section 6.

2. Simulation methodology

The tip-sample system is described by a 2D model such that electrostatics and current continuity equations are solved fully in 2D real space. In self-consistent calculations, the current continuity equations including tunnelling process are solved iteratively until convergence is achieved to obtain the terminal currents. The tunnelling current can also be obtained non self-consistently (in a post processing) for comparison. In practice, the non self-consistent solution for a bulk semiconductor (like p-GaAs) will be very close to the self-consistent solution of the current continuity equations as shown later.

A tunnelling current calculation within the direct quantum tunnelling model [12] takes place along parallel slices through the gap. The model is based on a formula for elastic tunnelling proposed by Tsu and Esaki [41], and further developed by Price and Radcliffe [39]. The current density J through a potential barrier is obtained according to the number of generated carriers using the following formula [20]:

$$J = \frac{qkT}{2\pi^2\hbar^3} m^* \int T(E) \times \ln\left[\frac{1 + \exp(E_{Fsamp} - E)/kT}{1 + \exp(E_{Ftip} - E)/kT} \right]$$ (1)

where E is the charge carrier energy, $m^* = \sqrt{m_x m_y}$ (where m_x and m_y are carrier effective masses in the lateral directions), $E_{F_{tip}}$ is the tip quasi-Fermi level and $E_{F_{samp}}$ is the sample quasi-Fermi level. The integration term is determined with respect to the band edge position for every bias point. In equilibrium, $E_{F_{samp}} = E_{F_{tip}}$ and the term J is equal to zero.

The transmission probability $T(E)$, defined as the ratio of transmitted and incident currents, is calculated by solving Schrödinger's equation in the effective mass approximation [42]. It was demonstrated in the past that these approximations are very accurate to describe the sample-tip system in STS [43] because electrons do not tunnel in to or from one specific energy level, instead using a broad band of energies decaying away exponentially from the Fermi level. This approach was found to be more accurate than the commonly used Wentzel-Kramers-Brillouin (WKB) approximation for the case of thin barriers for all energies [20].

The transmission probability $T(E)$ is obtained as [44] :

$$T(E) = \frac{2}{1 + g(E)} \qquad (2)$$

with

$$g(E) = \frac{\pi^2}{2} \frac{m_s k_m}{m_m k_s} \left(Bi'_d Ai_0 - Ai'_d Bi_0 \right)^2 +$$

$$+ \frac{\pi^2}{2} \frac{m_m k_s}{m_s k_m} \left(Bi_d Ai'_0 - Ai_d Bi'_0 \right)^2 +$$

$$+ \frac{\pi^2}{2} \frac{m_m m_s}{\lambda_0^2 m_i^2 k_s k_m} \left(Bi'_d Ai'_0 - Ai'_d Bi'_0 \right)^2 +$$

$$+ \frac{\pi^2}{2} \frac{\lambda_0^2 m_i^2 k_m k_s}{m_s m_m} \left(Bi_d Ai_0 - Ai_d Bi_0 \right)^2 + \qquad (3)$$

where m_m, m_s and m_i are effective electron masses in metal, semiconductor and insulator respectively, k_m and k_s are the wavevectors in metal and semiconductor, respectively, $\lambda_0 = \hbar\Theta_i / qF_i$, and A_i and B_i are the Airy functions defined as following:

$$Ai_0 \equiv Ai\left(\frac{\Phi_B - E}{\hbar\Theta_i} \right) \qquad (4)$$

$$Ai_d \equiv Ai\left(\frac{\Phi_B + qE_i d - E}{\hbar\Theta_i} \right) \qquad (5)$$

where $\hbar\Theta_i = \sqrt[3]{q^2 \hbar^2 F_i^2 / 2m_i}$, Φ_B is the barrier height for electrons or holes, E_i is electric field in insulator, and d is the insulator thickness [12,20].

The tip-sample structure (including air surrounding the metal tip) is 2.5 µm wide with the bulk semiconductor layer 0.9 µm deep. An example of the 2D circular tip structure with a regular triangular mesh is given in Figure 1(e), where the projection of the cylindrical tip into 2D assumes that the tip is uniform in the z-direction. We have checked, by numerical experiments, that a sufficient number of grid points is used in the tip-sample separating region in the direction of the current flow. Homogeneous (reflecting) Neumann boundary conditions are used at all simulation cell boundaries except contacts where the Dirichlet boundary conditions are used. The metal tip is assumed to be a contact. An additional contact is added at the bottom of the semiconductor to allow for current to flow. The current flow from the semiconductor through the insulator/air is via a tunnelling process only.

To examine the role of the image force, we implemented the tunnelling model by Schenk for ultrathin insulator layers [20]. The model accounts for the image force effects using a pseudobarrier method which calculates the transmission probability coefficient $T(E)$ (Equation 2) of the modified trapezoidal potential barrier. To evaluate the effective barrier height as a function of electron incident energy, the image force potential is calculated according to the formula by Kleefstra and Herman[45]:

$$E_{im}(x) = \frac{q^2}{16\pi\varepsilon_i} \sum_{n=0}^{\infty} (k_1 k_2)^n \times \left[\frac{k_1}{nd + x} + \frac{k_2}{d(n+1) - x} + \frac{2k_1 k_2}{d(n+1)} \right] \qquad (6)$$

where

$$k_1 = -1, \ k_2 = \frac{\varepsilon_i - \varepsilon_s}{\varepsilon_i + \varepsilon_s}$$

and ε the relative dielectric permittivity of insulator (ε_i) and semiconductor (ε_s) regions, d is the insulator thickness, and x is the position through the barrier.

The image force potential is added to the trapezoidal barrier potential. The model assumes the simple parabolic approximation of the barrier shape due to the fact that for a very thin potential barrier the error is negligible [46]. The barrier height is evaluated at three different energy levels as follows [12]:

$$\Phi(E) = \Phi(E_1) + \frac{\Phi(E_3) - \Phi(E_1)}{(E_3 - E_1)(E_2 - E_3)}(E - E_1)(E_2 - E) -$$

$$-\frac{\Phi(E_2) - \Phi(E_1)}{(E_2 - E_1)(E_2 - E_3)}(E - E_1)(E_3 - E) \qquad (7)$$

Table 1. The material parameters used in simulations.

Material	m_c, $[\times m_o]$	m_{hh}, $[\times m_o]$	m_{lh}, $[\times m_o]$	E_g, [eV]	Affinity, [eV]
GaAs	0.067	0.49	0.16	1.42	4.07
InP	0.0759	0.56	0.12	1.35	4.4
GaP	0.13	0.79	0.14	2.75	4.4
Al$_{0.3}$Ga$_{0.7}$As	0.092	0.571	0.157	1.8	3.75
In$_{0.53}$Ga$_{0.47}$As	0.045	0.532	0.088	0.734	4.67

The Schenk tunnelling current model was implemented both self-consistently and in post processing calculations. For thin rectangular tips, and circular tips, there is little difference between a self-consistent solution and simpler post processing calculations. The material parameters used in simulations can be found in Table I, where m_c is an effective mass in the conduction band, m_{hh} is a heavy hole effective mass, m_{lh} is a light hole effective mass and E_g is a band gap.

On the flat defect free (110) surface of III-V materials there are no surface state distributions centred in the bandgap and the surface can be modelled as bulk [22]. Nevertheless, the developed methodology allows a full treatment of surface states very straightforwardly and can be included in a wide range of ways from i) uniform distribution of defect states, via ii) realistic distribution either defined by iia) analytical functions (Gaussian, exponential) or even iib) a realistic distribution of surface states obtained experimentally, to introducing iii) interface traps .

3. Bandgap simulations for GaAs

To test the importance of the probe shape, several tip geometries were simulated, as shown in Figure 1. The discretised geometry of the finite element model allows any realistic tip shape. The triangular tip shape Figure 1(b) results in a slow convergence of calculations of tunnelling current at high voltages, while Figure 1(c) and Figure 1(d) give similar results, as seen in Figure 1(f). For reduced computational time Figure 1(c) is used for the results presented here, with a 70 nm tip radius, 1 nm tip-sample separation and a tip work function of 5 eV.
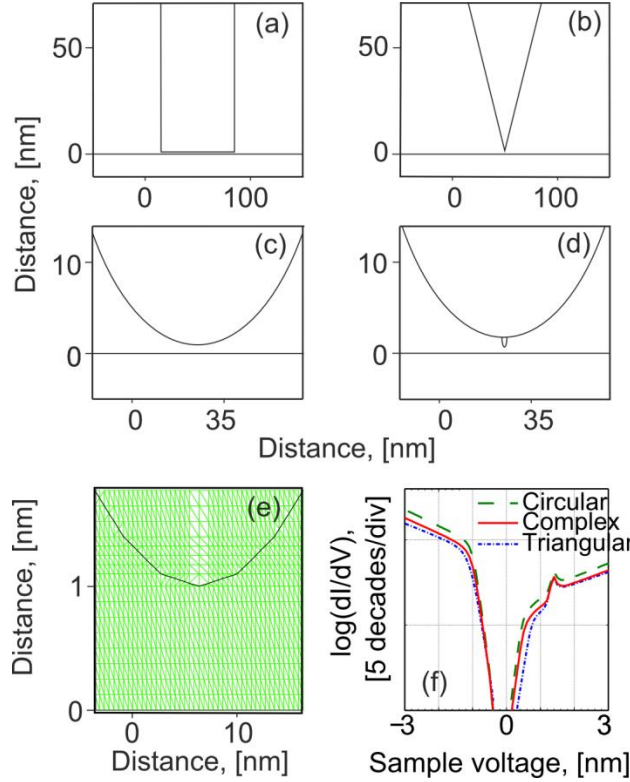
Fig 1: Probe tip in 2D of rectangular (a), triangular (b), circular (c) shapes, and realistic complex (d) shape with a large radius of 70 nm with a smaller tip on the top with a radius of 10 nm. (e) 2D circular tip structure with mesh.

Tunnelling spectra for n-type GaAs (n-GaAs) with a doping concentration of $N_D = 10^{18}$ cm^{-3} and $N_D = 10^{12}$ cm^{-3} are shown in Figure 2. For $N_D = 10^{12}$ cm^{-3} n-GaAs, the vertical solid lines at sample voltages of +1.5 V and -1.1 V indicate the onset of higher tunnelling outside of the bandgap region. Similarly, for $N_D = 10^{18}$ cm^{-3} n-GaAs, the lines at sample voltages of +0.65 V and -0.78 V indicate the bandgap by the onset of larger tunnelling.

The change of the apparent band gap with doping concentration in Figure 2 demonstrates the effect of tip-induced band bending. For the higher doped case, the onset of larger current corresponds to the tip crossing the valence and conduction band edges. In case of the low doping, the origin of the observed gap is not so straightforward. Therefore, the energy band alignment is shown in detail in Figure 3 for the onset voltages of +1.5 and -1.1 V. In Figure 3(a), the applied tip voltage has induced depletion and inverted the surface to make it appear p-type. The tip applied bias has to be beyond +1.5 V before a significant tip-to-sample tunnelling can take place. In Figure 3(b), the sample surface is in accumulation appearing more n-type than the bulk. The induced surface accumulation region has filled states in the conduction band (see Figure 3(b) inset) from which sample-to-tip tunnelling can take place before the tip crosses the valence band edge. This effect is described by Koenraad as Type I accumulation [22] . For $N_D = 10^{18}$ cm^{-3} n-GaAs, a bandgap of 1.43 eV is obtained from simulations, 0.01 eV larger than the true bandgap of 1.42 eV, which would be within the systematic error of experimental data [47]. The screening effect of the high doping reduces the amount of tip-induced band bending. For a doping of $N_D = 10^{12}$ cm^{-3} n-GaAs, tip-induced band bending increases the observed band gap to 2.60 eV. An onset in the tunnelling current spectra is visible in the conduction band around +2 V in the highly doped n-type GaAs marked by an arrow in Figure 2.
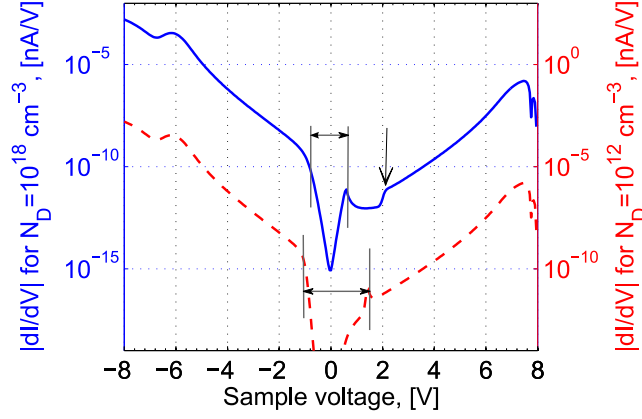
Fig 2: Tunnelling current spectra for the *n*-GaAs with a doping concentration of $N_D = 10^{18}$ cm^{-3} (blue solid line corresponds to the left scale) and $N_D = 10^{12}$ cm^{-3} (red dashed line corresponds to the right scale). The onsets of higher tunnelling in the CB and VB are marked with vertical lines.
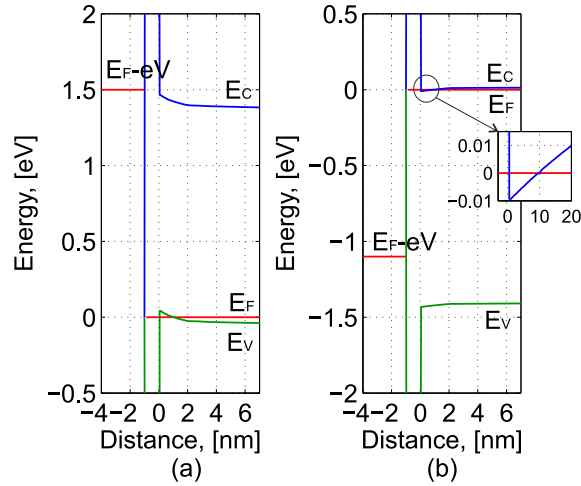

(a)   (b)

Fig 3: Energy band structure of the *n*-GaAs, $N_D = 10^{18}$ cm^{-3} obtained at sample voltages of +1.5 V (a) and -1.1 V (b).

Figure 4 shows the band edge in detail before and after the onset of the tunnelling current at +1.9 eV and +2.5 eV. At +2.5 eV, the surface inversion has bent the valence band above the sample Fermi level, allowing electrons to also tunnel from the tip to these empty inversion states. This is described by Koenraad as Type II inversion [22]. This induced depletion region is spatially localised under the tip. In Figure 4(c) and (d), the tunnelling current contributions from the valence and conduction bands are shown as a function of distance, with the tip at the origin, for the corresponding case shown in Figure 2. At +2.5 V, the valence band tunnelling increases in magnitude beyond the conduction band tunnelling. In all cases, the tunnelling current is larger under the tip and reduces almost exponentially as a function of the tip-surface distance.

The bandgap simulations for other semiconductor materials like InP, AlGaAs, InGaAs and GaP can be found in Appendix A.
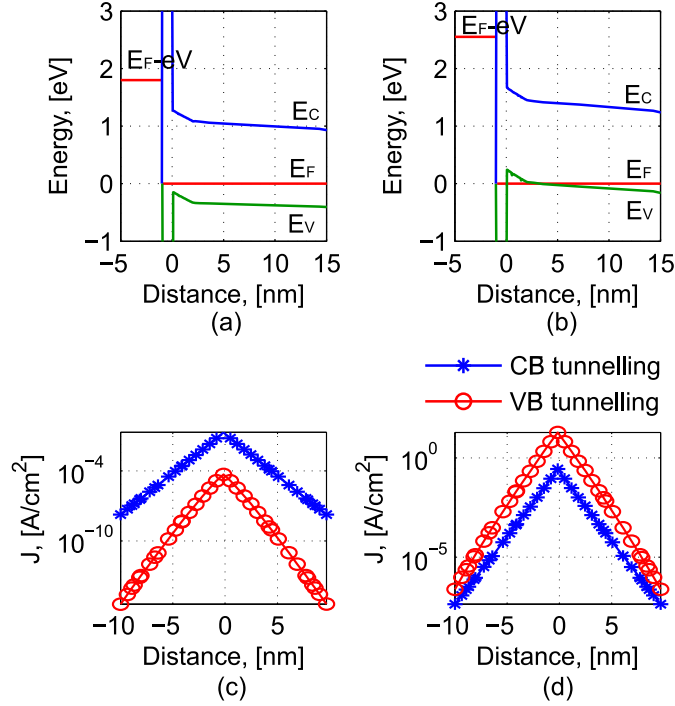
Fig 4: Energy band structure profiles at sample voltages of +1.9 V (a) and +2.5 V (b). Corresponding tunnelling current density from the conduction (blue stars) and valence (red open circles) bands at sample voltages of +1.9 V (c) and +2.5 V (d).

4. Comparison with experimental data and other models

Figure 5 compares the experimental data obtained from the STM measurements performed on *p*-type GaAs [17] with the simulated results from our approach and from the latest version of software Semitip 6 [48]. The Semitip model [49] is based on the Bardeen formalism using the Tersoff and Hamman approximation. The Bardeen model [34] assumes that the tunnelling current can be obtained from the difference in electron scattering rates of the tip and the semiconductor sample, which is equal to the number of sample or tip states weighted by their occupation probabilities, multiplied by their charge [50]. However, this model does not account for the effect of the image force, which is known to reduce the potential barrier for tunnelling and thus increase the current. Therefore, the tunnelling current obtained directly from the Semitip simulations was multiplied by three orders of magnitude to obtain an agreement with the experiment [17–19]. We investigate the effect of image force on conduction and valence bands in detail in Section 5.

A comparison with experimental results has been carried out using the following parameters taken from the Ref. [17] : a tip radius R=30 nm, a tip-sample separation s=0.9 nm, a contact potential $\Delta\varphi$=-1.4 eV, and 0.7 nm^2 area of the tunnel junction [17]. Figure 5 compares the current spectra as a function of applied tip bias for the latest version of Semitip 6 software and our model created with the same set of free parameters, to explain the differences in the models. Both models can be fitted exactly to the experimental data with another set of the parameters, for example with another value of contact potential and tip-sample separation.

One of the differences between the 2D models arises in the calculation of the magnitude of the tip-induced band bending. The surface potential energy directly under the tip apex was compared with the potential energy far inside the semiconductor for voltages from -2 V to +2 V as illustrated in Figure 6 for both Semitip 6 and our model in 2D and 3D. Both reproduce a large tip-induced band bending when the semiconductor is in depletion (negative sample voltage for *p*-type material) and a small band bending due to the screening effect of the

8

surface charge density when the semiconductor is in accumulation (positive sample voltage for *p*-type material). The difference in the potential computation for the valence band is one of the sources of the mismatch in the 2D models in Figure 5. This is due to the fact that a 2D model used by Atlas assumes that a 2D tip shape is extended in a third direction, while Semitip 2D model uses an azimuthal symmetry in cylindrical coordinates. When a full 3D model is used than the tip-induced band bending agrees with that of Semitip 2D calculations as shown in Figure 6.

The material parameters used in our simulations differ from those used by Feenstra. In Semitip, heavy hole effective mass m_{hh}=0.643m_o, light hole effective mass m_{lh}=0.081m_o, and split-off effective mass m_{so}=0.172m_o. The material parameters for GaAs used in the present work are summarized in Table 1. However, when the same parameters from Table 1 were used in Semitip, no significant difference was found.
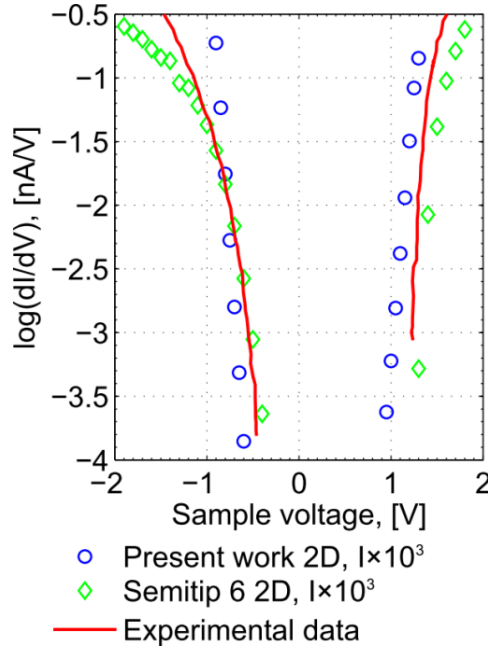

Fig 5: Simulation results from Semitip 6 model and present work compared against experimental spectra for *p*-GaAs with a doping concentration of $N_A = 10^{18}$ cm^{-3} [17]. Simulations were made with the same set of parameters to study the difference in the models. The current was increased by three orders of magnitude following procedure from Semitip 6 to account for the image charge induced barrier lowering. Both models can be fitted exactly to the experimental data with another set of the parameters for the of contact potential and tip-sample separation.
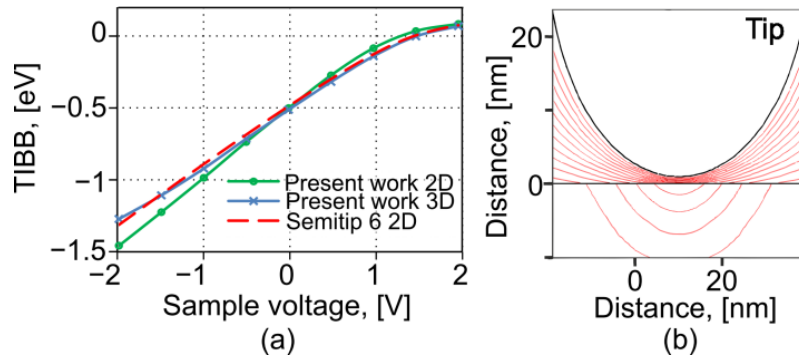

(a)   (b)

Fig 6: Comparison of tip-induced band bending models for present work and Semitip 6 model. (b) Potential distribution directly under the tip apex when no bias voltage is applied, contours are displaced by 0.1 V.

5. Image force simulations

The image force alternates the shape and lowers an ideal trapezoidal tunnelling barrier and thus increases the tunnelling current. One approximation to avoid performing computations with this complex barrier shape is to introduce a constant magnitude scaling factor for the tunnelling current which mimics the lowering of the height of triangular barrier, as it was used for Semitip in Section 4 [17–19]. It was shown by Schenk [20], that in case of the ultra-thin gate dielectrics in metal-oxide-semiconductor structures the common approximation of the image force brakes, and a new theory which can be used for other applications was developed. We use the Schenk tunnelling model to demonstrate the implication of the theory in case of STM in vacuum/air.

Figure 7 shows spectra with and without image force correction for a rectangular tip shape, similar to Figure 1(a) but with a width of 0.7 nm, and simplified circular tip shape with the radius 30 nm, similar to Figure 1(c), both separated by 0.9 nm from the p-GaAs surface with a doping concentration $N_A = 10^{18}$ cm^{-3}. There is a consistent four orders of magnitude increase in tunnelling current when the correction is included for the rectangular tip shape (see Figure 7(a)). Alternation of the tunnelling current through the conduction band (CB) due to the effect of image force is well known [18] so the previous models used a constant scaling factor for the tunnelling current considering the correction for CB only. We include the image force correction also for valence band (VB). This results in a very different impact on the CB and VB tunnelling currents for every bias point. With the same model applied to a circular tip, conduction band tunnelling current is found to be three orders of magnitude larger and the valence band tunnelling current six orders larger (see Figure 7(b)). The magnitude difference will change with the different structure parameters, tip shape, and semiconductor materials. The difference observed in the image force correction for circular and rectangular tip shapes might have a serious implication on the tunnelling current magnitude for models where a circular tip shape is approximated by a staircase, which is commonly used in the modelling of atomic force microscopy and Kelvin probe microscopy measurements [7,8].
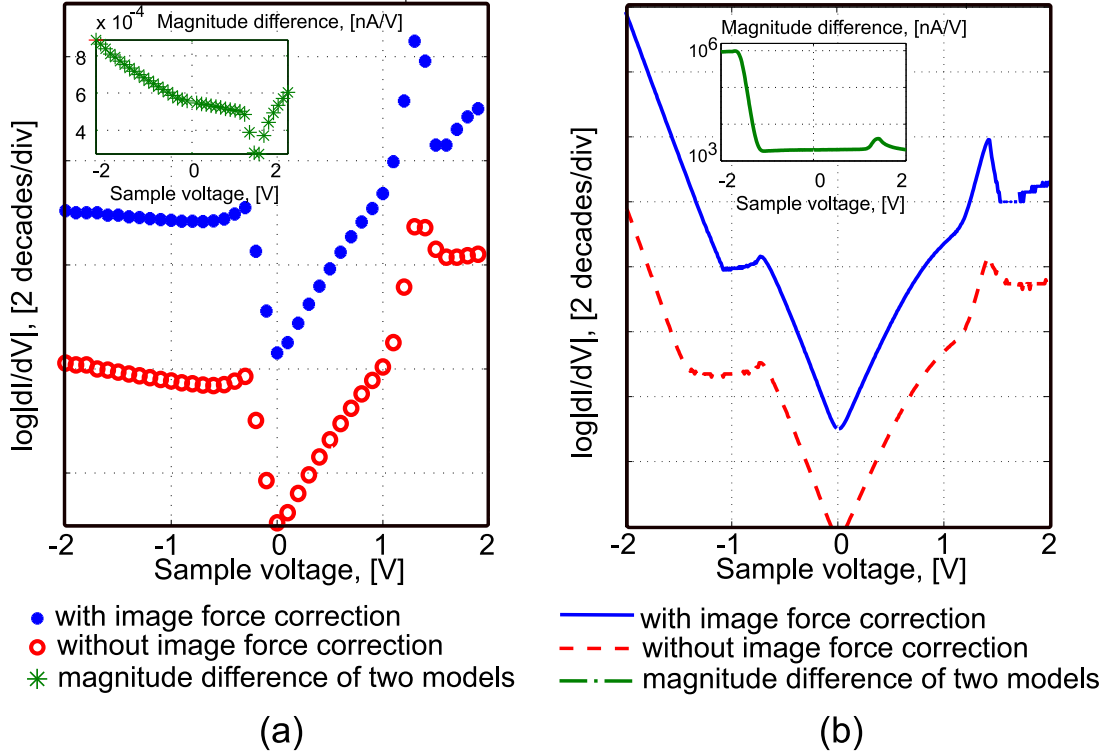
Fig 7: dI/dV spectra obtained when no image force correction is included in the model and when the image force correction is included for (a) rectangular tip shape and (b) circular tip shape. The insets show the magnitude difference in the currents when the image force correction is included and not included.

6. Conclusion

An STM and STS simulation methodology based on the Price and Radcliffe tunnelling formalism using image force correction has been developed using the Silvaco *ATLAS*. This 2D finite element model was applied to several semiconductor materials to verify its accuracy, with the origin of features in the spectra examined in detail. The simulations confirmed that, at larger doping concentrations, the screening effect of the semiconductor reduces the tip-induced band bending. For *n*-type GaAs, the modelled spectra bandgap deviates from the bulk value by only 0.1 eV or 0.7 % which is within the experimental systematic error [47]. At low *n*-type doping concentrations, the screening is weak, and tip-induced band bending causes the apparent bandgap to either increase or reduce depending on the tunnelling mechanism. These phenomena well justify the need for STM and STS modelling to accompany the experimental measurements. The Poisson-Schrödinger solver in our 2D model predicts a larger tip-induced band bending when a sample is in depletion (resulting in a shift of the band onset in the spectra), than that from Semitip 2D, and the same amount of tip-induced band bending when a full 3D model is used.

The image force correction gives a conduction band tunnelling current increase of three orders of magnitude, and a valence band tunnelling current increase of six orders, compared to the 'artificial' uniform increase of three orders of magnitude used in Ref. [17]. The magnitude change is different for different tip shapes and sample materials.

Finally, our STM model developed within a commercial simulation tool offers several advantages over other STM models. These advantages include i) the ability to use any realistic tip shape, ii) to include full device transport models for SPM on devices, and iii) to model spectra from SPM on powered devices. The model can also account for surface states, and can readily be extended to other SPM techniques.

11

Appendix A. Bandgap simulations for InP, AlGaAs, InGaAs and GaP
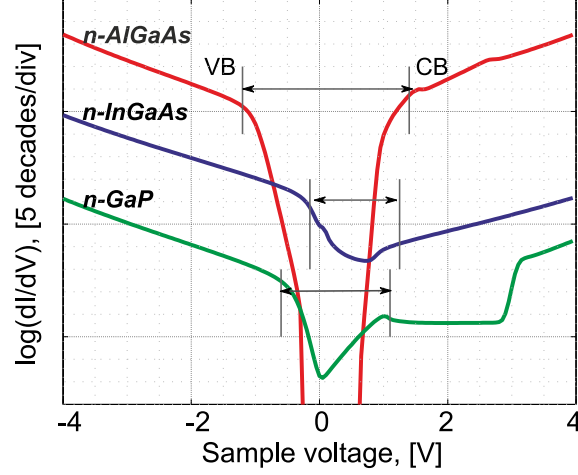
Fig A.8: Tunnelling spectra of the $Al_{0.3}Ga_{0.7}As$, $In_{0.53}Ga_{0.47}As$ and GaP with $N_D = 10^{16}$ cm^{-3}.

The simulation methodology was applied to $Al_{0.3}Ga_{0.7}As$, $In_{0.53}Ga_{0.47}As$ and GaP, all with a doping concentration of $N_D = 10^{16}$ cm^{-3}. All material parameters used in the simulations can be found in Table 1. These simulations used a 70 nm tip radius, 1 nm tip-sample separation and a tip work function of 4.7 eV. For this intermediate n-type doping, Figure A.8 shows that modelled band gaps are 2.6 eV for $Al_{0.3}Ga_{0.7}As$ compared to the experimental value of 1.8 eV, and 1.4 eV instead of 0.734 eV for $In_{0.53}Ga_{0.47}As$, both due to tip-induced band bending delaying the onset of increased current. For GaP, the apparent bandgap was 1.7 eV instead of 2.75 eV due to Type I accumulation as seen earlier. A kink-like feature is also seen in the spectrum of GaP at +3 V, when Type II depletion shifts to Type II inversion [22], and tunnelling in to the valence band dominates over tunnelling in to the conduction band.

To demonstrate the modelling for a p-type material, p-type InP with a doping concentration of $N_A = 10^{12}$ cm^{-3} is shown in Figure A.9 using the same tip-sample structure parameters and tip work function 5 eV. The observed band gap of 2.85 eV is larger than the experimental bandgap of 1.42 eV due to large amount of the tip-induced band bending in the low doped material, when the screening effect of the doping is weak.
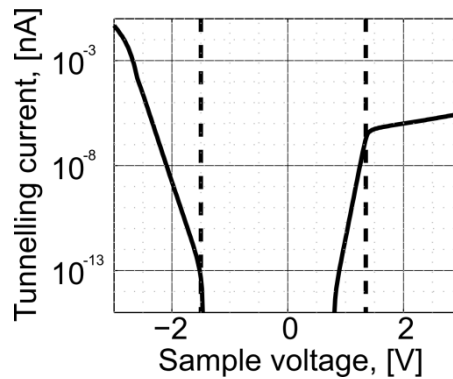
Fig A.9: Simulated tunnelling spectra for p-InP. The vertical dashed lines correspond to the onsets of the larger tunnelling in the conduction and valence bands.

References

[1]   E. Meyer, Scanning probe microscopy and related methods., Beilstein J. Nanotechnol. 1 (2010) 155–7.

[2]   R.J. Cobley, K.S. Teng, M.R. Brown, P. Rees, S.P. Wilks, Surface defects in semiconductor lasers studied with cross-sectional scanning tunneling microscopy, Appl. Surf. Sci. 256 (2010) 5736–5739.

[3]   S. Saraf, Y. Rosenwaks, Local measurement of semiconductor band bending and surface charge using Kelvin probe force microscopy, Surf. Sci. 574 (2005) L35–L39.

[4]   R.J. Cobley, P. Rees, K.S. Teng, S.P. Wilks, Analyzing real-time surface modification of operating semiconductor laser diodes using cross-sectional scanning tunneling microscopy, J. Appl. Phys. 107 (2010) 094507.

[5]   A. Lochthofen, W. Mertin, G. Bacher, L. Hoeppel, S. Bader, J. Off, et al., Electrical investigation of V-defects in GaN using Kelvin probe and conductive atomic force microscopy, Appl. Phys. Lett. 93 (2008) 22107.

[6]   L. Koenders, A. Yacoot, Tip Geometry and Tip-Sample Interactions in Scanning Probe Microscopy (SPM), in: W. Osten (Ed.), Fringe 2005, Springer Berlin Heidelberg, 2006: pp. 456–463.

[7]   S. Sadewasser, T. Glatzel, R. Shikler, Y. Rosenwaks, M.C. Lux-Steiner, Resolution of Kelvin probe force microscopy in ultrahigh vacuum: comparison of experiment and simulation, Appl. Phys. Lett. 210 (2003) 32–36.

[8]   E. Koren, N. Berkovitch, O. Azriel, A. Boag, Y. Rosenwaks, E.R. Hemesath, et al., Direct measurement of nanowire Schottky junction depletion region, Appl. Phys. Lett. 99 (2011) 223511.

[9]   D. Ziegler, P. Gava, J. Güttinger, F. Molitor, L. Wirtz M. Lazzeri, A. M. Saitta, et al., Variations in the work function of doped single- and few-layer graphene assessed by Kelvin probe force microscopy and density functional theory, Phys. Rev. B. 83 (2011) 235434.

[10] S. Fremy, S. Kawai, R. Pawlak, T. Glatzel, A. Baratoff, E. Meyer, Three-dimensional dynamic force spectroscopy measurements on KBr(001): atomic deformations at small tip-sample separations, 23 (2012) 55401.

[11] ITRS Reports, 2012.

[12] SILVACO ATLAS User's Manual, 2007.

[13] R. J. Cobley, K. S. Teng, M. R. Brown, S. P. Wilks, P. Rees, Direct real-time observation of catastrophic optical degradation in operating semiconductor lasers using scanning tunneling microscopy, Appl. Phys. Lett. 91 (2007) 81119.

[14]   T.J. Kempa, B. Tian, D.R. Kim, J. Hu, X. Zheng, C.M. Lieber, Single and tandem axial p-i-n nanowire photovoltaic devices., Nano Lett. 8 (2008) 3456–60.

[15]   W. Wu, S. L. Skala, J. R. Tucker, J. W. Lyding, A. Seabaugh, E. A. Beam, et al., Interface characterization of an InP/InGaAs resonant tunneling diode by scanning tunneling microscopy, J. Vac. Sci. Technol., A. 13 (1995) 602–606.

[16]   A. Gurlo, M. Ivanovskaya, Grain size control in nanocrystalline In 2 O 3 semiconductor gas sensors, Sensors Actuators B …. 44 (1997) 327–333.

[17]   R.M. Feenstra, Y. Dong, M.P. Semtsiv, W.T. Masselink, Influence of tip-induced band bending on tunnelling spectra of semiconductor surfaces, Nanotechnology. 18 (2007) 44015.

[18]   J.G. Simmons, Generalized Formula for the Electric Tunnel Effect between Similar Electrodes Separated by a Thin Insulating Film, J. Appl. Phys. 34 (1963) 1793.

[19]   G. Binnig, N. Garcia, H. Rohrer, J.M. Soler, F. Flores, Electron-metal-surface interaction potential with vacuum tunneling: Observation of the image force, Phys. Rev. B. 30 (1984) 4816–4818.

[20]   A. Schenk, G. Heiser, Modeling and simulation of tunneling through ultra-thin gate dielectrics, J. Appl. Phys. 81 (1997) 7900–7908.

[21]   R.M. Feenstra, J.A. Stroscio, Tunneling spectroscopy of the GaAs(110) surface, J. Vac. Sci. Technol. B. Microelectron. Nanom. Struct. 5 (1987) 923–929.

[22]   G.J. de Raad, D. Bruls, P. Koenraad, J. Wolter, Interplay between tip-induced band bending and voltage-dependent surface corrugation on GaAs(110) surfaces, Phys. Rev. B. 66 (2002) 1–14.

[23]   S. Loth, M. Wenderoth, R. Ulbrich, S. Malzer, G. Döhler, Connection of anisotropic conductivity to tip-induced space-charge layers in scanning tunneling spectroscopy of p-doped GaAs, Phys. Rev. B. 76 (2007) 1–10.

[24]   M. Hirayama, J. Nakamura, A. Natori, Band-bending effects on scanning tunneling microscope images of subsurface dopants: First-principles calculations, J. Appl. Phys. 105 (2009) 083720.

[25]   R. Feenstra, Electrostatic potential for a hyperbolic probe tip near a semiconductor, J. Vac. Sci. Technol. B …. 2080 (2003) 1–17.

[26]   R. Feenstra, J. Lee, M. Kang, G. Meyer, K. Rieder, Band gap of the Ge (111) c (2× 8) surface by scanning tunneling spectroscopy, Phys. Rev. B. 035310 (2006) 1–29.

[27]   Vienna Ab-initio Simulation Package User's Manual, 2013.

[28]   ACCELRYS User's Manual, 2013.

[29]   ATOMISTIX User's Manual, 2013.

[30]   P. Hohenberg, W. Kohn, Inhomogeneous Electron Gas, Phys. Rev. 136 (1964) B864–B871.

[31]   W. Kohn, L.J. Sham, Self-Consistent Equations Including Exchange and Correlation Effects, Phys. Rev. 140 (1965) A1133–A1138.

[32]   M. V Fischetti, S.E. Laux, Monte Carlo study of electron transport in silicon inversion layers, Phys. Rev. B. 48 (1993) 2244–2274.

[33]   V.A. Ukraintsev, Data evaluation technique for electron-tunneling spectroscopy, Phys. Rev. B. 53 (1996) 11176–11185.

[34]   J. Bardeen, Tunnelling from a many-particle point of view, Phys. Rev. Lett. 6 (1961) 6–8.

[35]   G.D. Mahan, Many-Particle Physics, 2nd ed., Plenum Press, 1983.

[36]   N. Isshiki, K. Kobayashi, M. Tsukada, First-principle simulation of scanning tunneling microscopy/spectroscopy with cluster models of W, Pt, TiC, and impurity adsorbed tips, in: Proc. Fifth Int. Conf. Scanning Tunneling Microsc., AVS, 1991: pp. 475–478.

[37]   J.M. Bass, C.C. Matthai, Scanning-tunneling-microscopy and spectroscopy simulation of the GaAs(110) surface, Phys. Rev. B. 52 (1995) 4712–4715.

[38]   B.W. Hoogenboom, C. Berthod, M. Peter, Ø. Fischer, Modeling scanning tunneling spectra of $Bi_{2}Sr_{2}CaCu_{2}O_{8+\delta}$, Phys. Rev. B. 67 (2003) 1–7.

[39]   P. Price, J. Radcliffe, Esaki tunneling, IBM J. Res. Dev. (1959).

[40]   C.K. Egan, A. Choubey, A.W. Brinkman, Scanning tunneling microscopy and spectroscopy of the semi-insulating CdZnTe(110) surface, Surf. Sci. 604 (2010) 1825–1831.

[41]   R. Tsu, L. Esaki, Tunneling in a finite superlattice, Appl. Phys. Lett. 22 (1973) 562–564.

[42]   D.K. Ferry, Semiconductors, Macmillan, 1991.

[43]   R.M. Feenstra, Electrostatic potential for a hyperbolic probe tip near a semiconductor, J. Vac. Sci. Technol., B. 21 (2003) 2080–2088.

[44]   K.H. Gundlach, Zur berechnung des tunnelstroms durch eine trapezförmige potentialstufe, Solid. State. Electron. 9 (1966) 949–957.

[45]   M. Kleefstra, G.C. Herman, Influence of the image force on the band gap in semiconductors and insulators, J. Appl. Phys. 51 (1980) 4923.

[46]   R. Stratton, Volt-current characteristics for tunneling through insulating films, J. Phys. Chem. Solids. 23 (1962) 1177–1190.

[47]   R. Feenstra, Tunneling spectroscopy of the (110) surface of direct-gap III-V semiconductors, Phys. Rev. B. 50 (1994).

[48]   N. Ishida, K. Sueoka, R. Feenstra, Influence of surface states on tunneling spectra of n-type GaAs(110) surfaces, Phys. Rev. B. 80 (2009) 1–8.

[49]   R. Feenstra, S. Gaan, Quantitative Determination of Nanoscale Electronic Properties of Semiconductor Surfaces by Scanning Tunnelling Spectroscopy, J. Phys. Conf. Ser. 326 (2011) 012009.

[50]   A.D. Gottlieb, L. Wesoloski, Bardeen's tunnelling theory as applied to scanning tunnelling microscopy: a technical guide to the traditional interpretation, Nanotechnology. 17 (2006) R57.